Article

Fabrication and Characterization of an Optimized Low-Loss Two-Mode Fiber for Optoacoustic Sensing

Zelin Zhang [1,2]**, Guanglei You** [3]**, Yu Qin** [1,2]**, Jianqin Peng** [4]**, Shuhong Xie** [5]**, Xinli Jiang** [5]**, Caoyuan Wang** [2]**, Ruowei Yu** [2]**, Yichun Shen** [1,*] **and Limin Xiao** [2,*]

[1] Zhongtian Technology Advanced Materials Co., Ltd., Zhongtian Technology Group, Nantong 226010, China
[2] Advanced Fiber Devices and Systems Group, Key Laboratory of Micro and Nano Photonic Structures (MoE), Key Laboratory for Information Science of Electromagnetic Waves (MoE), Shanghai Engineering Research Center of Ultra-Precision Optical Manufacturing, School of Information Science and Technology, Fudan University, Shanghai 200433, China
[3] Zhongtian Technology Fiber Co., Ltd., Zhongtian Technology Group, Nantong 226010, China
[4] College of Physics, Nanjing University of Aeronautics and Astronautics, Nanjing 210016, China
[5] Zhongtian Technology Group, Nantong 226463, China
[*] Correspondence: shenyc@chinaztt.com (Y.S.); liminxiao@fudan.edu.cn (L.X.)

Abstract: An optimized multi-step index (MSI) 2-LP-mode fiber is proposed and fabricated with low propagation loss of 0.179 dB/km, low intermodal crosstalk and excellent bend resistance. We experimentally clarified the characteristics of backward Brillouin scattering (BBS) and forward Brillouin scattering (FBS) induced by radial acoustic modes ($R_{0,m}$) in the fabricated MSI 2-LP-mode fiber, respectively. Via the use of this two-mode fiber, we demonstrated a novel discriminative measurement method of temperature and acoustic impedance based on BBS and FBS, achieving improved experimental measurement uncertainties of 0.2 °C and 0.019 kg/(s·mm^2) for optoacoustic chemical sensing. The low propagation loss of the sensing fiber and the new measurement method based on both BBS and FBS may pave the way for long-distance and high spatial resolution distributed fiber sensors.

Keywords: few-mode fiber; Brillouin scattering; optoacoustic interaction; optoacoustic chemical sensing

1. Introduction

Few-mode fibers (FMFs), due to their potential to raise the transmission capacity, have attracted intensive attention in optical communications and advanced sensors [1–3]. Combined with the space division multiplexing (SDM) technique, the FMF, as one of the key specialty fibers, is addressing the impending transportation "capacity crunch" by adding more spatial channels with several linear polarized (LP) modes within a single fiber [3,4]. In order to achieve mode division multiplexed transmission efficiently in a complex circumstance, the requirements for such an FMF should be low attenuation, low intermodal crosstalk between the LP groups of modes, low differential mode group delay (DMGD) caused by different propagation constant of the respective LP modes and good bending resistance. By controlling the Alpha value of the refractive index profile (RIP) precisely, the graded index (GI) FMFs can achieve low DMGD and low intermodal crosstalk [5,6]. However, it is difficult for the GI-FMF to maintain the transmission attenuation at a low level (<0.19 dB/km) [1].

In order to provide a promising FMF for long-haul SDM transmission, in our work, by optimizing fiber RIP design and drawing processes, we fabricate an optimized multi-step index (MSI) 2-LP-mode fiber with low fiber attenuation, low intermodal crosstalk and ultra-low bending loss. Furthermore, in order to explore the potential of the proposed FMF in Brillouin scattering-based fiber sensors, we theoretically and experimentally investigate its Brillouin gain spectrum (BGS) and forward Brillouin scattering spectrum (FBSS) induced by

radial acoustic modes ($R_{0,m}$). Furthermore, by measuring its frequency shift dependencies of BGS and $R_{0,m}$-induced FBSS on temperature and acoustic impedance, respectively, we demonstrate this optimized MSI 2-LP-mode fiber as a new sensing fiber for optoacoustic sensing and propose a novel simultaneous measurement method of temperature and acoustic impedance based on FBS and BBS with low measurement uncertainties.

2. Low-Loss MSI 2-LP-Mode Fiber

A trench-assisted multi-step designed refractive index profile (RIP) of the 2-LP-mode fiber is shown in Figure 1, which consists of a central core with a high refractive index embedded in the large core with a low refractive index and a refractive index trench around the whole fiber core. The design strategies of our optimized FMF are applied from refs. [3,6]. The DMGD and effective index difference (δ_{neff}) between the fundamental (LP$_{01}$) and first higher-order mode (LP$_{11}$) can be controlled by adjusting the Δ_k value precisely. By depressing the d_2/d_1 ratio properly, the effective area (A_{eff}) can be increased. Next, the trench volume (Δ_t) can be optimized to minimize the bending loss for these two guided LP modes while maintaining high losses for the higher-order leaky LP modes to ensure effective cut-off. Finally, an optimized RIP is obtained, where the values of Δ_k, Δ_t and d_2/d_1 are 4.2×10^{-3}, 9.1×10^{-3} and 1.8, respectively.
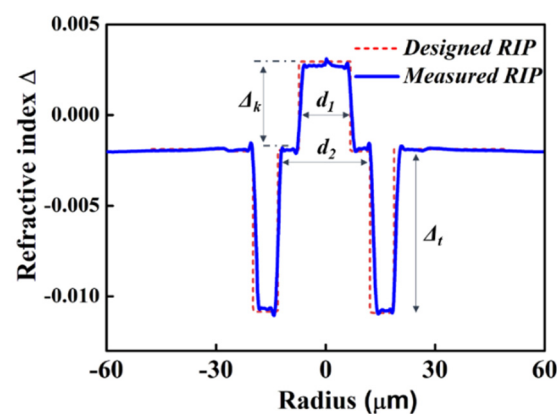

Figure 1. Designed and measured refractive index profile of MSI 2-LP-mode fiber.

The preform of 2-LP-mode fiber is developed with MCVD to match the designed index profile closely. The fiber core is crafted from silica doped with germania, and the trench is made from silica with fluorine. Different from GI few-mode fibers [5–8], the drawing processes of this 2-LP-mode fiber have been optimized to obtain better geometrical uniformity and lower attenuation. The furnace is precisely controlled at a higher heating temperature of 2095 °C. Using the constant drawing tension control process, we use the lower drawing tension, which is maintained at 70 ± 3 g. The preform is drawn into the fiber under the optimized drawing speed (300 m/min). The key parameters of the MSI 2-LP-mode fiber, such as α (Fiber attenuantion@1550 nm), A_{eff} (Effective mode area), D (Dispersion coefficient), DMGD (Differential mode group delay), δ_{neff} (Effective index difference between LP$_{01}$ and LP$_{11}$ @1550 nm) and B_L (Micro-bending loss @1550 nm), are shown in Table 1.

As shown in Table 1, using the optical time domain reflectometry (OTDR), the measured attenuation at 1550 nm of 0.179 dB/km is much lower than the value of 0.198 dB/km in ref. [7]. By optimizing the Δ_k value, the δ_{neff} between LP$_{01}$ and LP$_{11}$ can reach up to 2.6×10^{-3}, which is two times higher than that of the two-mode fiber reported in ref. [8]. Additionally, the DMGD value can decrease to 1.9 ps·m^{-1}. In particular, the obtained MSI 2-LP-mode fiber has excellent bend resistance. When the 10 turns are introduced with the bend radius of 5 mm, the measured B_L value is less than 0.006 dB at 1550 nm. Furthermore, the effective areas of LP$_{01}$ and LP$_{11}$ are both above 130 µm^2 in Table 1, which make the fiber suitable for increasing the nonlinear thresholds for long-haul transmission [9].

Table 1. Parameters of the MSI 2-LP-mode Fiber.

Parameter	Value
α (dB/km)	0.179
Diameter of cladding (μm)	125.1
Diameter of coating (μm)	245.3
LP$_{01}$ mode A_{eff} @1550 nm (μm^2)	133
LP$_{11}$ mode A_{eff} @1550 nm (μm^2)	147
LP$_{01}$ mode D (ps·nm^{-1}·km^{-1})	22.8
LP$_{11}$ mode D (ps·nm^{-1}·km^{-1})	21.2
(LP$_{11}$–LP$_{01}$) δ_{neff}@1550 nm	2.6×10^{-3}
(LP$_{11}$–LP$_{01}$) DMGD (ps·m^{-1})	1.9
B_L [dB, 10 turns @ R (Bending radius) = 5 mm]	$\leq$0.006

3. BBS and FBS Effects in MSI 2-LP-Mode Fiber

As shown in Table 1, the optimized MSI 2-LP-mode fiber, due to its low fiber attenuation, low intermodal crosstalk and low bending loss, can act as a good candidate for long-haul optical communication. Meanwhile, its capacities based on Brillouin scattering are also desirable to be investigated in the fields of optical sensors. As a result, we will explore the BBS and FBS processes, respectively, in the MSI 2-LP-mode fiber and demonstrate its potential application in Brillouin scattering-based optical sensors.

3.1. BBS Effect in MSI 2-LP-Mode Fiber

The BBS in optical fibers is a nonlinear process where a propagating optical wave can interact with longitude acoustic waves to produce backscattered waves [10]. The BBS process can be described using the following 2D scalar equation group [9]

$$\nabla^2 E(x,y) + \left(\frac{2\pi}{\lambda}\right)^2 (n^2 - n_{eff}^2) E(x,y) = 0, \tag{1}$$

$$\nabla^2 u(x,y) + \left(\frac{\omega_a^2}{V_L^2} - \beta_a^2\right) u(x,y) = 0, \tag{2}$$

where $E(x,y)$ and $u(x,y)$ are the electric field of optical mode and the displacement field of acoustic modes, respectively. The parameter λ is the wavelength of the optical mode in a vacuum. Additionally, ω_a, V_L and β_a are the angular frequency, the velocity of longitudinal acoustic mode and the propagation constant of longitude acoustic modes, respectively. Using the finite element analysis (FEA) method and solving Equation (1), the electric field distributions at 1550 nm of two LP modes supported by the MSI 2-LP-mode fiber can be theoretically obtained, which are shown in Figure 2. The two-dimensional mode profiles of two LP modes in the direction of A to B are both shown in Figure 2b.
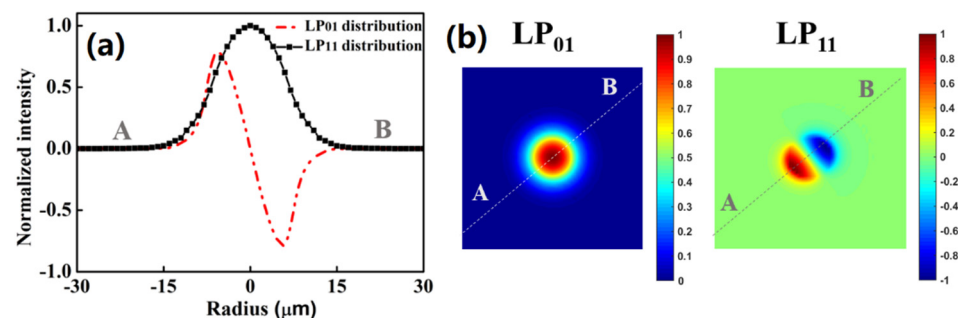

Figure 2. Calculated electric fields of guided LP mode LP$_{01}$ and LP$_{11}$ at 1550 nm in the optimized MSI 2-LP-mode fiber. (**a**) Two-dimensional mode profiles, and (**b**) electric field mode pattern.

By solving Equations (1) and (2), the four acoustic modes, named A1, A2, A3 and A4, are calculated and shown in Figure 3. It can be found that these four acoustic modes are circular symmetrical and confined in the fiber core. The higher-order acoustic modes, A2, A3 and A4, may derive from the sharp rise and fall of the index profile of 2-LP-mode fiber between the center core and the edge of the larger core [11].
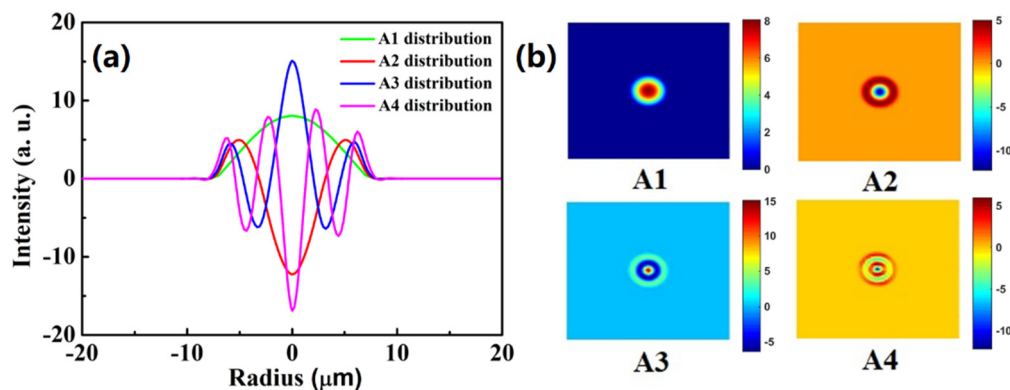

Figure 3. (**a**) Two-dimensional (2D) mode profiles and (**b**) field patterns of four acoustic modes.

When several acoustic modes are excited in the fiber simultaneously, each acoustic mode is responsible for a spectral feature in the Brillouin gain spectrum (BGS). The BGS corresponding to the *i*th acoustic mode can be expressed as [12]

$$g_i(v) = g_i \cdot \frac{(\Delta v/2)^2}{(v - v_i)^2 + (\Delta v/2)^2} \tag{3}$$

$$v_i = \frac{2n_{eff}V_{eff}^i}{\lambda} \tag{4}$$

where Δv, v_i and g_i are the full width at half maximum (FWHM), central frequency shift and peak Brillouin gain of the *i*th acoustic mode-induced BGS, respectively. Additionally, V_{eff}^i is the effective acoustic velocity of the *i*th acoustic mode.

According to Equation (3), each acoustic mode-induced BGS has a Lorentzian shape. The total BGS is the sum of the BGSs of individual acoustic modes, which can be expressed as [13]

$$g_B(v) = \sum_i g_i(v) \tag{5}$$

By solving Equations (1)–(5), the obtained numerical BGS of the optimized MSI 2-LP-mode fiber is shown in Figure 4. It can be observed that the intensity of the first peak is more than 23 dB higher than that of the second peak. The intensities of the third and fourth peak are both less than −35 dB. As shown in Figures 2 and 3, the highest intensity of the first peak can be explained by the fact that the field distribution of A1 acoustic mode tends to concentrate more towards to fiber core, which can strengthen the optoacoustic interaction between A1 and LP01 modes. The second, third and fourth Brillouin resonance peaks are so weak that the total BGS of the optimized MSI 2-LP-mode fiber has a single-peak Lorentzian shape. Furthermore, it can be calculated that the Brillouin frequency shift (BFS) and FWHM of the main peak are 10.712 GHz and 31 MHz, respectively.
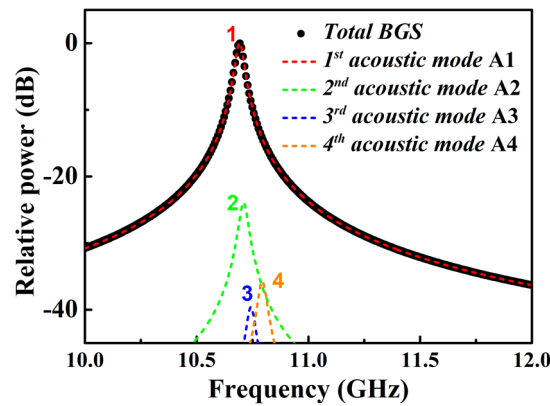
Figure 4. Numerical results of BGS of the MSI 2-LP-mode fiber.

3.2. FBS Effect in MSI 2-LP-Mode Fiber

As one of the typical optoacoustic interactions in optical fiber, the FBS process is caused by transverse acoustic modes, which involve radial acoustic modes ($R_{0,m}$) and mixed torsional–radial acoustic modes ($TR_{2,m}$), different from BBS induced by longitudinal acoustic waves [14]. However, due to the random variation of polarization states of the beam propagating along the non-polarization-maintaining fiber, the FBS induced by $TR_{2,m}$ modes is much weaker than that induced by $R_{0,m}$ modes [15]. Therefore, the FBS characteristics of the MSI 2-LP-mode fiber corresponding to the $R_{0,m}$ modes are investigated.

Driven by the electrostriction effect in fibers [16], the $R_{0,m}$ modes are excited, which gives rise to spatiotemporal changes in the refractive index. Due to the photo-elastic effect, these changes in the refractive index can induce the pure phase modulation to the optical wave and produce the forward-scattered stokes wave [15]. Therefore, the total FBS process can be described as the coupling amplitude equations between the optical field of optical wave E (r, z, t) and acoustic wave for the displacement vector U (r, z, t) [16,17]

$$\nabla^2 E - \frac{n_{eff}^2}{c^2}\frac{\partial^2 E}{\partial t^2} = \frac{1}{\varepsilon_0 c^2}\frac{\partial^2 P_{NL}}{\partial t^2}, \tag{6}$$

$$\frac{\partial^2 U}{\partial t^2} + \Gamma\frac{\partial U}{\partial t} + (\eta V_L)^2 \nabla \times (\nabla \times U) - V_L^2 \nabla(\nabla \cdot U) = F/\rho_0, \tag{7}$$

where P_{NL}, ε_0, c and ρ_0 are the total nonlinear polarization, vacuum permittivity, light velocity in vacuum and density of fused silica, respectively. The parameter η is the ratio between shear sound velocity and longitudinal sound velocity, and Γ is the acoustic damping parameter. $F = \varepsilon_0[1/2 \cdot \gamma_{12}\nabla(E \cdot E) + \gamma_{44}(E \cdot \nabla)E]$ is the electrostrictive driving term, where γ_{12} and γ_{44} are both the elements of the electrostrictive tensor for fused silica. By solving Equations (6) and (7), the normalized displacement distribution $U_m(r)$ of $R_{0,m}$ mode in the MSI 2-LP-mode fiber can be calculated as

$$U_m(r) = \frac{J_1\left[v_f r/(2\pi V_L)\right]}{\sqrt{2\pi \int \{J_1[v_f r/(2\pi V_L)]\}^2 r dr}} \tag{8}$$

where J_1 is the first-order Bessel function. The resonance frequency v_f of $R_{0,m}$ mode can be expressed as [18]

$$v_f = \frac{h_m V_L}{2\pi r_a} \tag{9}$$

where h_m is the eigenvalue of $R_{0,m}$ mode under the boundary condition corresponding to the free fiber surface, and r_a is the radius of fiber cladding. Using $\rho_m(r) = -\rho_0 \nabla U_m(r)$, the density vibration of $R_{0,m}$ modes also can be obtained. Taking the $R_{0,7}$ mode as example, the density vibration of the $R_{0,7}$ mode and spatial distribution is shown in Figure 5.
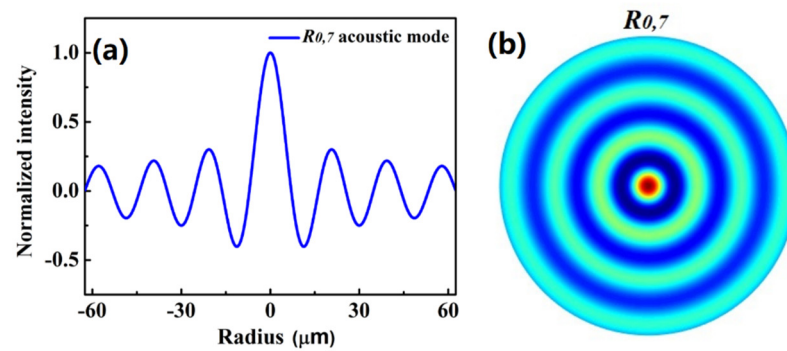
Figure 5. (**a**) The density vibration profile and (**b**) spatial distribution of $R_{0,7}$ mode.

We also experimentally measure the FBSS of the MSI 2-LP-mode fiber using a Sagnac loop, and the measured results are shown in Figure 6. It can be found that the resonance frequencies of $R_{0,m}$ modes in the MSI 2-LP-mode fiber are equally spaced with a spacing of 47.03 MHz. By solving Equations (6), (7) and (9), the calculated resonance frequency of $R_{0,7}$ mode is 322.7 MHz, which agrees well with the measured result of 319.7 MHz in Figure 6.
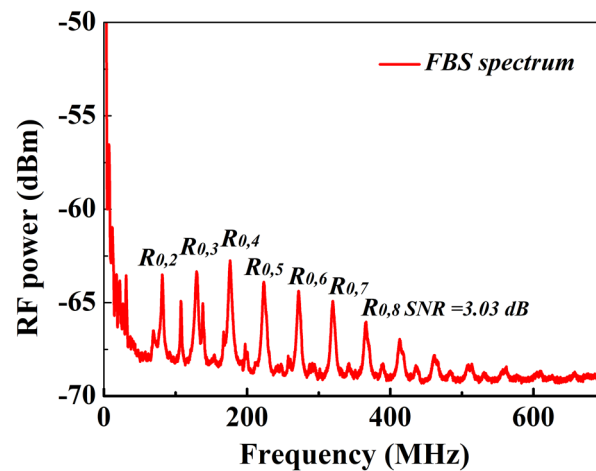

Figure 6. The measured FBS spectrum (FBSS) in the MSI 2-LP-mode fiber.

Furthermore, compared with the BGS in the MSI 2-LP-mode fiber, the FBS process involves multiple acoustic modes, and the FBSS shows a multi-peak shape. These characteristics may provide some possibilities for multi-parameter optical sensors based on Brillouin scattering, such as temperature, strain and acoustic impedance and so on [14,19]. Next, using the spectral dependencies of BGS and FBSS on temperature and acoustic impedance simultaneously, we experimentally demonstrate the feasibility of this optimized MSI 2-LP mode fiber as a new sensing fiber in optoacoustic chemical sensors.

4. Discriminative Sensing of Temperature and Acoustic Impedance by Using the MSI 2-LP-Mode Fiber

To date, temperature and acoustic impedance simultaneous measurement methods based on FBS have been reported to use the resonance frequencies of two $R_{0,m}$-induced FBS spectra [14] or the linewidth and resonance frequency of one $R_{0,m}$-induced FBSS [20]. However, due to the limited spatial resolutions and sensing distances of FBS-based distributed acoustic impedance (~2 m and ≤3 km) [21,22] and temperature (~42.5 m and ≤0.4 km) [23] sensing techniques, it is not easy to achieve the medium/long-distance distributed acoustic impedance and temperature simultaneous measurement with a high spatial resolution using these two sensing methods. Here, combined with BBS and FBS effects in the MSI 2-LP-mode fiber, we propose a novel discriminative measurement method of temperature and acoustic impedance with small measurement uncertainties, which may provide the

possibility to achieve longer sensing distance or higher spatial resolution by introducing BBS-based distributed mechanism for distributed acoustic impedance and temperature simultaneous measurement [24,25].

　　We experimentally investigate the frequency shift dependencies of BGS and $R_{0,m}$-induced FBSS on temperature and acoustic impedance in the MSI 2-LP-mode fiber, respectively. The experimental setup is shown in Figure 7. The laser source is a 1552 nm single-wavelength fiber laser with a linewidth of 15 kHz and output power of 8.2 dBm. After passing through an isolator (ISO), erbium-doped fiber amplifier (EDFA) and bandpass filter (BPF), the pump light is injected into the fiber Sagnac loop composed of a polarization controller (PC), a fiber under test (FUT) made of an uncoated 30 m-long MSI 2-LP-mode fiber and a 2 × 2 fiber coupler. In our experiment, the optical gain of EDFA is adjusted to 11.2 dB, and its noise figure is suppressed to 5 dB. The BPF has an ultra-narrow 3 dB bandwidth (<3 GHz) and high optical signal-to-noise (<50 dB) so that it can filter the amplified spontaneous emission (ASE) noise from EDFA as much as possible. The insertion loss of BPF is 2.1 dB. In the FUT, the excited $R_{0,m}$ modes and longitude acoustic modes can both apply acousto-optic phase modulation to the propagating light [15]. Then, the fiber Sagnac interferometer can convert these two types of phase modulation into intensity modulation, which will be detected by a photo-detector (PD) with 12.5 GHz bandwidth. Finally, the lower-frequency FBS spectrum and higher-frequency BGS can be simultaneously observed and analyzed by an electrical spectrum analyzer (ESA). The frequency range of ESA is from 1 Hz to 26.5 GHz, and the spectrum is averaged 500 times.
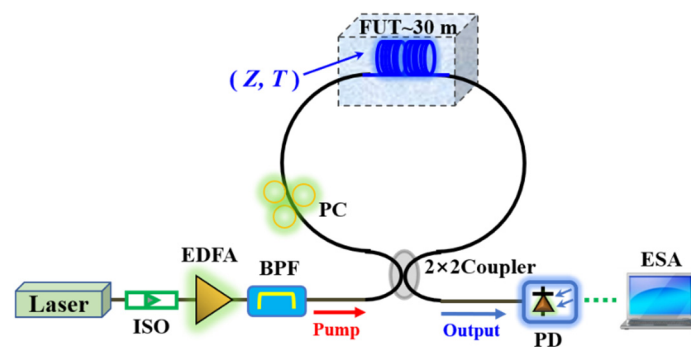

Figure 7. Experimental setup for observing BGS and FBSS in the MSI 2-LP-mode fiber.

　　Firstly, the MSI 2-LP-mode fiber is placed into a water bath to measure the FBS spectra and BGS as a function of temperature, respectively. As shown in Figure 6, taking consideration of the signal-to-noise ratio (SNR) and $R_{0,m}$ modes induced FBS spectra dependencies on temperature (note that some low-order $R_{0,m}$ modes exhibit the higher SNRs but lower frequency shift-coefficients [14]), the $R_{0,7}$-induced FBSS is selected to investigate its frequency shift dependencies on temperature. As shown in Figure 8a,b, it can be clearly observed that, within the range from 0 to 50 °C, the frequency shift dependencies of $R_{0,7}$-induced FBSS and BGS on temperature show the linear relationships with the different frequency shift-temperature coefficients of $C_{v\text{-}T\_7}$ = 25 kHz/°C and $C_{v\text{-}T\_B}$ = 1.05 MHz/°C, respectively.

　　Secondly, the FUT is immersed into the sucrose solution with different mass fractions of sucrose, which are from 0 to 50% with steps of 10%. The temperature of the sucrose solution is kept constant at room temperature (~20 °C). The relationship between the concentration of sucrose solution and acoustic impedance can be found in ref. [26]. From Figure 9a, it can be found that, with increasing acoustic impedance, the central frequency of $R_{0,7}$-induced FBSS linearly shifts to high frequency with a coefficient ($C_{v\text{-}Z\_7}$) of 0.301 MHz/[kg/(s·mm²)]. Interestingly, a new feature can be observed that the measured central frequency of BGS remains nearly constant when the acoustic impedance is changed to 2.02 kg/(s·mm²). It means that the BGS is insensitive to the changes in acoustic impedance, and the frequency shift-acoustic impedance coefficient ($C_{v\text{-}Z\_B}$) can be

approximately expressed as zero. As shown in Figure 3, this feature can be explained by the fact that the total longitude acoustic modes and BBS process are confined in the fiber core, which can be isolated from external matter.
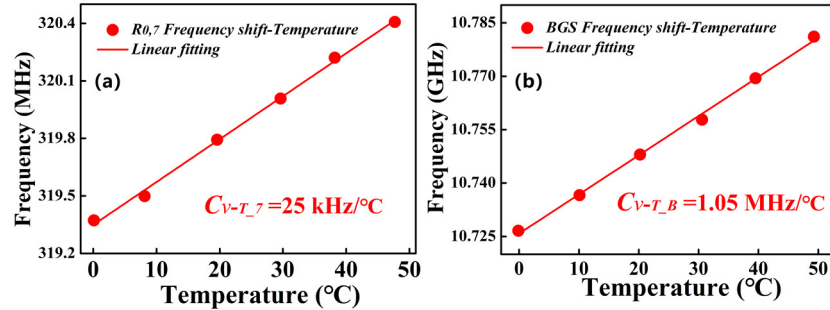

Figure 8. Frequency shift for (**a**) $R_{0,7}$-induced FBSS and (**b**) BGS as a function of temperature.
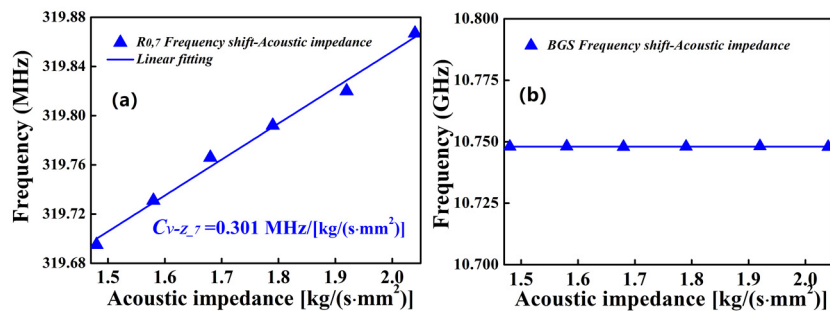

Figure 9. Frequency shift for (**a**) $R_{0,7}$-induced FBSS and (**b**) BGS as a function of acoustic impedance.

Different from refs. [14,20], the abovementioned experimental results in which the impedance $R_{0,7}$-induced FBSS and BGS have their individual frequency shift dependencies on temperature and acoustic impedance may provide a novel discriminative measurement method of temperature and acoustic impedance.

When the acoustic impedance and temperature are changed simultaneously, both of them can cause the frequency shifts of $R_{0,7}$-induced FBSS and BGS ($\Delta\nu_7$ and $\Delta\nu_B$), respectively. Thus, these can be expressed as

$$\Delta\nu_7 = C_{\nu-T\_7}\cdot\Delta T + C_{\nu-Z\_7}\cdot\Delta Z \tag{10}$$

and

$$\Delta\nu_B = C_{\nu-T\_B}\cdot\Delta T + C_{\nu-Z\_B}\cdot\Delta Z \tag{11}$$

where the ΔT and ΔZ are the changes in temperature and acoustic impedance, respectively. The measurement uncertainties of the central frequencies of $R_{0,7}$-induced FBSS and BGS ($\delta\nu_7$ and $\delta\nu_B$) are, respectively,

$$\delta\nu_7 = C_{\nu-T\_7}\cdot\delta T + C_{\nu-Z\_7}\cdot\delta Z \tag{12}$$

and

$$\delta\nu_B = C_{\nu-T\_B}\cdot\delta T + C_{\nu-Z\_B}\cdot\delta Z \tag{13}$$

where the δT and δZ are the measurement uncertainties of temperature and acoustic impedance. Using Equations (12) and (13), the δT and δZ can be expressed as

$$\delta T = \frac{\sqrt{(C_{\nu-Z\_B}\cdot\delta\nu_{F\_7})^2 + (C_{\nu-Z\_7}\cdot\delta\nu_B)^2}}{|C_{\nu-Z\_B}C_{\nu-T\_7} - C_{\nu-T\_B}C_{\nu-Z\_7}|} \tag{14}$$

and

$$\delta Z = \frac{\sqrt{(C_{\nu-T\_B} \cdot \delta \nu_{F\_7})^2 + (C_{\nu-T\_7} \cdot \delta \nu_B)^2}}{|C_{\nu-Z\_B} C_{\nu-T\_7} - C_{\nu-T\_B} C_{\nu-Z\_7}|} \tag{15}$$

In order to compare our experiment with the existing results in the literature more conveniently, the 40 °C distilled water (the corresponding acoustic impedance is 1.505 kg/(s·mm^2) [27]) is set as State 1, and the 20% sucrose solution (the corresponding acoustic impedance is 1.689 kg/(s·mm^2) [26]) is set as the State 2. The actual temperatures of these two measured states are controlled at 40.1 °C and 20.1 °C, respectively. In our experiment, the measurement uncertainties of $R_{0,7}$-induced FBSS and BGS can be obtained by calculating the standard deviation of seven measured results [14,20], which are 1.6 kHz and 157 kHz, respectively. Figure 10a,c show the measured $R_{0,7}$-induced FBSS at State 1 and State 2, where the corresponding central frequencies (ν_{7_0} and ν_{7_R}) are respectively 320.211 MHz and 319.766 MHz, respectively. Figure 10b,d show the measured $R_{0,7}$-induced FBSS at State 1 and State 2, where the corresponding central frequencies (ν_{B_0} and ν_{B_R}) are 10.769 GHz and 10.748 GHz, respectively.
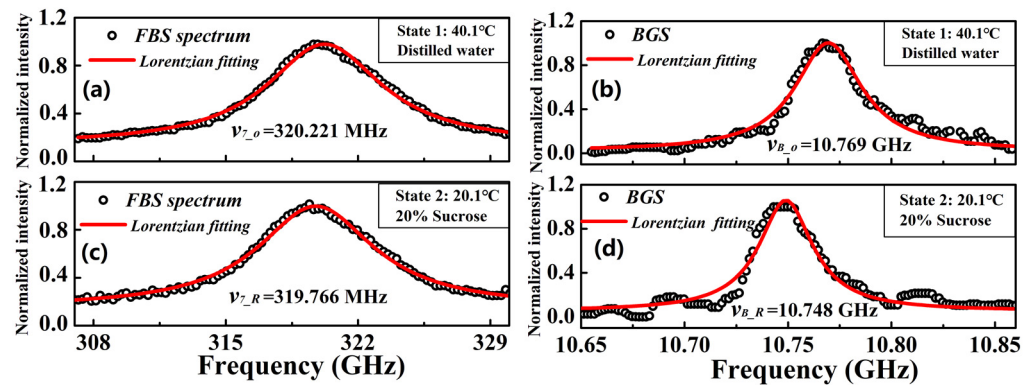

Figure 10. The measured induced FBSS induced by radial acoustic mode of (**a**) $R_{0,7}$ at State 1 and (**c**) $R_{0,7}$ at State 2 as well as BGS at (**b**) State 1 and (**d**) State 2.

By regarding State 1 as the original state and solving Equations (10) and (11), the temperature and acoustic impedance at State 2 can be obtained as T_{R_e} = 19.9 °C and Z_{R_e} = 1.670 kg/(s·mm^2), respectively. Therefore, the experimental measurement uncertainties of temperature ($\delta T_e = |T_{R\_e} - T_R|$) and acoustic impedance ($\delta Z_e = |Z_{R\_e} - Z_R|$) are 0.2 °C and 0.019 kg/(s·mm^2), respectively. Moreover, by solving Equations (12)–(15), the theoretical measurement uncertainties of temperature (δT) and acoustic impedance (δZ) can be calculated as 0.15 °C and 0.014 kg/(s·mm^2), respectively. These differences between theoretical and experimental measurement uncertainties may originate from the evaluated errors of linear coefficients. Compared with the experimental results in ref. [14], the proposed novel temperature and acoustic impedance simultaneous measurement method based on FBS and BBS in the optimized MSI 2-LP-mode fiber can achieve more than 36% accuracy improvements.

5. Conclusions

In conclusion, by optimizing RIP design and drawing processes, we can successfully fabricate an optimized MSI 2-LP-mode fiber with low fiber attenuation, low mode coupling and ultra-low bending loss. Then, we can theoretically and experimentally investigate the characteristics of $R_{0,m}$-induced FBS and BGS and clarify their frequency shift dependencies on temperature and acoustic impedance in the MSI 2-LP-mode fiber. By utilizing these relationships, we have proposed and verified a novel simultaneous measurement method of temperature and acoustic impedance based on FBS and BBS. The obtained measurement uncertainties of temperature and acoustic impedance are only 0.2 °C and 0.019 kg/(s·mm^2), respectively, achieving more than 36% accuracy improvements. In the future, combined

with BBS-based distributed mechanisms, such as differential pulse-width pair [24], optical pulse coding [25] and in-line Raman amplification [28], the optimized MSI 2-LP-mode will be a new sensing fiber to achieve longer sensing distance or higher spatial resolution for distributed acoustic impedance and temperature simultaneous measurement, which would have potential applications in environmental engineering, chemical engineering and oil–gas reservoirs [14,20]. Furthermore, by employing multiple-input multiple-output (MIMO) and/or combining with a multi-core fiber structure [29,30], the proposed low-loss FMF will also be a good candidate for long-haul mode-division-multiplexing (MDM) and/or SDM to achieve a large enhancement of transmission capacity per optical fiber in the future.

Author Contributions: Conceptualization, Z.Z., G.Y., Y.S. and L.X.; methodology, Z.Z. and J.P.; software, C.W. and R.Y.; validation, Z.Z. and J.P.; formal analysis, Y.Q. and Z.Z.; investigation, S.X. and X.J.; writing—original draft preparation, Z.Z.; writing—review and editing, L.X. and Y.S.; funding acquisition, L.X. All authors have read and agreed to the published version of the manuscript.

Data Availability Statement: All the data presented in this study are available in this article.

Conflicts of Interest: The authors declare no conflict of interest.

References

1. Pierre, S.; Denis, M.; Marianne, B.A.; Koen, D.J.; Frank, A.; Amado, M.V.; Rodrigo, A.; Chigo, M.O. Low-Differential-Mode-Group-Delay 9-LP-Mode Fiber. *J. Lightwave Technol.* **2016**, *34*, 425–430.
2. Li, A.; Wang, Y.F.; Hu, Q.; Shieh, W. Few-mode fiber based optical sensors. *Opt. Express* **2015**, *23*, 1139–1150. [CrossRef] [PubMed]
3. Koebele, C.; Salsi, M.; Sperti, D.; Tran, P.; Brindel, P.; Mardoyan, H.; Bigo, S.; Boutin, A.; Verluise, F.; Sillard, P.; et al. Two mode transmission at 2x100Gb/s, over 40km-long prototype few-mode fiber, using LCOS-based programmable mode multiplexer and demultiplexer. *Opt. Express* **2011**, *19*, 16593–16600. [CrossRef] [PubMed]
4. Koonen, A.M.J.; Chen, H.S.; Sleiffer, V.A.J.M.; Uden, R.G.H.V.; Okonkwo, C.M. Compact integrated solutions for mode de-multiplexing. In Proceedings of the OECC/ACOFT, Melbourne, Australia, 6–10 July 2014.
5. Li, M.J.; Hoover, B.; Li, S.P.; Bickham, S.; Ten, S.; Ip, E.; Huang, Y.K.; Mateo, E.; Shao, Y.; Wang, T. Low Delay and Large Effective Area Few-Mode Fibers for Mode-Division Multiplexing. In Proceedings of the 17th Opto-Electronics and Communications Conference, Busan, Korea, 2–6 July 2012.
6. Pierre, S.; Denis, M. Few-Mode Fibers for Mode-Division-Multiplexed Systems. *J. Lightwave Technol.* **2014**, *32*, 2824–2829.
7. Nielsen, L.G.; Sun, Y.; Nicholson, J.M.; Jakobsen, D.; Jespersen, K.G.; Pálsdóttir, B. Few-Mode Transmission Fiber with Low DGD, Low Mode Coupling, and Low Loss. *J. Lightwave Technol.* **2012**, *30*, 3693–3698. [CrossRef]
8. Jespersen, K.; Li, Z.; Nielsen, G.; Pálsdóttir, B.; Poletti, F.; Nicholson, J.W. Measuring Distributed Mode Scattering in Long, Few-Mode Fibers. In Proceedings of the OFC/NFOEC, Los Angeles, CA, USA, 4–8 March 2012.
9. Zhang, Z.Z.; Lu, Y.G.; Pan, Y.H.; Bao, X.Y.; Chen, L. Trench-assisted multimode fiber used in Brillouin optical time domain sensors. *Opt. Express* **2019**, *27*, 11396–11405. [CrossRef] [PubMed]
10. Bao, X.Y.; Chen, L. Recent Progress in Brillouin Scattering Based Fiber Sensors. *Sensors* **2011**, *11*, 4152–4187. [CrossRef]
11. Xu, Y.; Ren, M.; Lu, Y.; Lu, P.; Bao, X.; Wang, L.; Messasseq, Y.; Larochelle, S. Multi-parameter sensor based on stimulated Brillouin scattering in inverse-parabolic graded-index fiber. *Opt. Lett.* **2016**, *41*, 1138–1141. [CrossRef]
12. Agrawal, G.P. *Nonlinear Fiber Optics*, 4th ed.; Academic Press: New York, NY, USA, 2006; pp. 353–358.
13. Ke, W.W.; Wang, X.J.; Tang, X. Stimulated Brillouin Scattering Model in Multi-Mode Fiber Lasers. *IEEE J. Sel. Top. Quantum Electron.* **2014**, *20*, 0901610.
14. Zhang, Z.Z.; Lu, Y.G.; Tanaka, Y.; Peng, J.Q.; Zhuang, Z.K. Discriminative sensing of temperature and acoustic impedance by using forward Brillouin scattering in large effective area fiber. *Appl. Phys. Express* **2021**, *14*, 042004. [CrossRef]
15. Nishizawa, N.; Kume, S.; Mori, M.; Goto, T. Experimental analysis of guided acoustic wave Brillouin scattering in PANDA fibers. *J. Opt. Soc. Am. B* **1995**, *12*, 1651–1655. [CrossRef]
16. Biryukov, A.S.; Sukharev, M.E.; Dianov, E.M. Excitation of sound waves upon propagation of laser pulses in optical fibres. *Quantum Electron.* **2002**, *32*, 765–775. [CrossRef]
17. Kang, M.S.; Brenn, A.; Russell, P.S.J. All-Optical Control of Gigahertz Acoustic Resonances by Forward Stimulated Interpolarization Scattering in a Photonic Crystal Fiber. *Phys. Rev. Lett.* **2010**, *105*, 153901. [CrossRef] [PubMed]
18. Picholle, E.; Picozzi, A. Guided-acoustic-wave resonances in the dynamics of a stimulated Brillouin fiber ring laser. *Opt. Commun.* **1997**, *135*, 327–330. [CrossRef]
19. Liu, X.; Bao, X.Y. Brillouin Spectrum in LEAF and Simultaneous Temperature and Strain Measurement. *J. Lightwave Technol.* **2012**, *30*, 1052–1057. [CrossRef]

20. Zhang, Z.Z.; Lu, Y.G.; Peng, J.Q.; Ji, Z.Y. Simultaneous measurement of temperature and acoustic impedance based on forward Brillouin scattering in LEAF. *Opt. Lett.* **2021**, *46*, 1776–1779. [CrossRef]

21. Pang, C.; Hua, Z.J.; Zhou, D.W.; Zhang, H.Y.; Chen, L.; Bao, X.Y.; Dong, Y.K. Opto-mechanical time-domain analysis based on coherent forward stimulated Brillouin scattering probing. *Optica* **2020**, *7*, 176–183. [CrossRef]

22. Bashan, G.; Diamandi, H.H.; London, Y.; Preter, E.; Zadok, A. Optomechanical time-domain reflectometry. *Nat. Commun.* **2020**, *7*, 176–183. [CrossRef]

23. Kato, Y.; Wada, Y.; Mizuno, Y.; Nakamura, K. Pilot demonstration of correlation-domain distributed temperature sensing using forward Brillouin scattering. *Jpn. J. Appl. Phys.* **2020**, *59*, 088002.

24. Li, W.H.; Bao, X.Y.; Li, Y.; Chen, L. Differential pulse-width pair BOTDA for high spatial resolution sensing. *Opt. Express* **2008**, *16*, 21616–21624. [CrossRef] [PubMed]

25. Soto, M.A.; Floch, S.L.; Thevenaz, L. Bipolar optical pulse coding for performance enhancement in BOTDA sensors. *Opt. Express* **2013**, *21*, 16390–16397. [CrossRef]

26. Saneyoshi, J.; Kikuchi, Y.; Nomoto, O. *Handbook of Ultrasonic Technology*; Cho-onpa Gijutsu Binran: Nikkan, Kogyo, 1978.

27. Marsh, J.N.; Hall, C.S.; Wickline, S.A.; Lanza, G.M. Temperature dependence of acoustic impedance for specific fluorocarbon liquids. *J. Acoust. Soc. Am.* **2002**, *112*, 2858–2862. [CrossRef] [PubMed]

28. Mohamed, N.A.; Yuh, T.C.; Trevor, P.N. 150-km-range distributed temperature sensor based on coherent detection of spontaneous Brillouin backscatter and in-line Raman amplification. *J. Opt. Soc. Am. B* **2005**, *22*, 1321–1324.

29. Shibahara, K.; Lee, D.; Kobayashi, T.; Mizuno, T.; Takara, H.; Sano, A.; Kawakami, H.; Miyamoto, Y.; Ono, H.; Oguma, M.; et al. Dense SDM (12-Core ×3-Mode) transmission over 527 km with 33.2 ns mode-dispersion employing low-complexity parallel MIMO frequency-domain equalization. *J. Lightwave Technol.* **2016**, *34*, 196–204. [CrossRef]

30. Ryf, R.; Randel, S.; Gnauck, A.H.; Bolle, C.; Sierra, A.; Mumtaz, S.; Esmaeelpour, M.; Burrows, E.C.; Essiambre, R.J.; Winzer, P.J.; et al. Mode-Division Multiplexing over 96 km of few-mode fiber using coherent 6 × 6 MIMO processing. *J. Lightwave Technol.* **2012**, *30*, 521–531. [CrossRef]